

Effects of Bio-joint Models on Compliant Exoskeleton Design

Kok-Meng Lee, *Fellow, IEEE/ASME*, and Jiajie Guo

Abstract— This paper presents a method taking advantage of medically available MRI (Magnetic Resonance Imaging) data to derive the kinematics of a knee joint. The bio-joint model is applied to the design of a compliant sensing mechanism with two examples. The first investigates the effect of materials and characteristic geometry of the compliant mechanism on the knee joint, while the second (utilizing the bio joint model as boundary conditions to measure the knee joint rotation and internal forces involved) provides a better understanding on the interaction between the human knee and compliant sensing mechanism. The results potentially help establish a new topic of accommodating human bio-joint variations and nature degrees-of-freedom movements in the design of an exoskeleton.

Keywords: compliant mechanism, exoskeleton, dynamic model, flexible beam, knee joint sensor

I. INTRODUCTION

Kinetics and kinematics analysis of joints are among the key topics in the research of exoskeleton. Most exoskeleton design analyses generally base on engineering joints rather than the natural bio-joints for which exoskeleton robots are designed to assist. Human bodies, however, vary widely in shapes and sizes, and also changes over years, rigid engineering parts often are not compliant to accommodate these variations. It has been noticed in [1] that ankle joint movements were greatly perturbed as soon as the exoskeleton power was added, causing significantly increased plantar flexion during stance. As a result, exoskeleton cannot be developed independently of studies of real bio joints.

With the rapid advances in mechatronics and robotics, exoskeletons have widely been developed to assist or rehabilitate human body motions; for example, the commercialized Lokomat [2] that has actuated hip and knee joint for the treadmill training. The BLEEX (Berkeley lower extremity exoskeleton) [3] enables people to carry heavy loads over rough terrain. Another robot suit called HAL (Hybrid assistive Limb) [4] was also developed to assist walking and climbing. An ankle-foot orthosis powered by artificial pneumatic muscles was developed in [5]. A shoulder exoskeleton was also designed to help elderly persons' daily life [6]. The Master II-ND developed at Rutgers is a force-feedback haptic glove using pneumatic actuators for the finger joints [7].

While exiting rehabilitation robots have the advantages of gaining energy in human motions and adjusting motion

patterns (e.g. treadmill training), there are potential damages to human joints in long term usage because rigid joints are often not designed to account for natural joint motion variations.

Compliant mechanisms that reduce assembled joints resulting in reduced frictions and increased energy efficiency can be employed in exoskeleton designs to accommodate shape/size/motion variation of human joints. In [8], "soft" pneumatic Muscle Actuators (pMA) were used as power source to achieve the lightness. The LOPES [9] was designed using flexible cable transmission. However, most of the work on compliance is motivated by power efficiency rather than the interaction between the human body and the exoskeleton. Recent works also concern about shock absorption, for example, a flexible geared joint and a rubber footpad [10]. Besides energy gained from the robots, it is essential that the exoskeleton should not interfere negatively to the normal human joint motions; otherwise, it will result in discomfort potential long term damage. For these reasons, problems on interaction between bio joints and compliant mechanism are worthy of exploration.

With MRI technology, joint details based on simple geometries (such as multi-circle/plane approximations) are available for studies [11]. To produce more informative model of kinematics and kinetics, it is desired that the models are mathematically differentiable. For this reason, the remainder of this paper offers the followings:

1. Motivated by the interests to understand the effect of modeling bio-joints [12][13] as engineering joints on the internal contact forces, we present a bio-joint model to analyze the flexion and the associated internal forces and torque within the joint. This model relaxes the commonly used engineering pin assumptions and thus, offers a more realistic approximation to predict the joint motion. The bio-joint model (that provides a means to account for the transitional motion interacting with rotation within the clearance of the joint) has been validated by comparing simulations against published MRI data [11].
2. We offer a design method utilizing a three dimensional (3D) compliant half-circle mechanism to measure the knee rotational angle, and determine the internal force/torque within the knee. The effects of materials and aspect ratios of the sensing mechanism on the human knee joint are numerically analyzed with boundary conditions derived from the knee joint model.

Although the analyses are in the context of a human knee joint, the results presented here can be extended to other type of bio-joints.

Manuscript received February 15, 2009. This work was supported in part by the Georgia Agricultural Technology Research Program (ATRP).

The authors are with the Woodruff School of Mechanical Engineering at Georgia Institute of Technology, Atlanta, GA 30332-0405 USA.

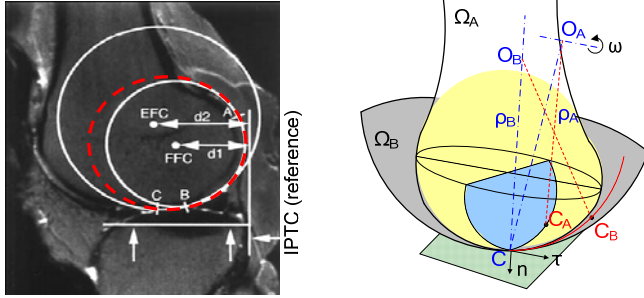
* Corresponding author, 404-894-7402; kokmeng.lee@me.gatech.edu

II. DYNAMIC MODEL OF HUMAN KNEE JOINT

Unlike an engineering pin or ball joint, a biological joint (Bio-joint) consists of non-uniform shaped contact parts and often with a significant clearance between them. With MRI data (see for example, [11]), a bio-joint model can be built for a human knee joint to provide a better understanding of knee kinematics and kinetics, and estimate the contact location and rolling/sliding velocities, and the force and torques involved.

A. Bio-joint model for a human knee

Figure 1(a) shows a lateral sagittal MR image of an unloaded cadaver knee [11], where the two white circles are approximated geometries for the femoral articular surfaces. Figure 1(b) represents a more general representation of a bio-joint as discussed in [12], where Ω_A and Ω_B are two bodies with surfaces Γ_A and Γ_B respectively. As shown in Fig. 1(b), Ω_A rolls on Ω_B ; and C is an instantaneous contact point. The angular velocity ω describes the motion of Ω_A at C. For the knee joint described in Fig. 1(a), $\omega = d\theta/dt$ where θ is the flexion angle. It is worth noting that the rotation axis is always changing as the contact point moves. The contact point on Γ_A and Γ_B moves incrementally from C_A and C_B to C along the respective osculating circles as shown in Fig. 1(b), where (O_A, ρ_A) and (O_B, ρ_B) are the centers and radii of the osculating circles contacting Γ_A and Γ_B respectively. The three dimensional (3D) motion of a biological joint can be characterized in the instantaneous osculating plane that depends on the location of the contact point.



(a) MRI of a cadaver knee [11] (b) Bio-joint model [12]
Fig. 1. Bio joint Illustration

Although data are presented as positions of the two (circle) centers denoted as EFC and FFC in Fig. 1(a), it is also valid to regard the contact occurred at points between a circle and a plane. To provide a continuous differentiable function, an alternative geometry based on an ellipse (red-dashed) is proposed to characterize the observed data. The effect of approximated geometries (circles and ellipse rolling on a flat plane) on the contact point position is analyzed as follows.

For the knee joint shown in Fig. 1(a), the rolling velocity v_{roll} is calculated as

$$v_{roll}(\theta) = \omega \rho_A \quad (1)$$

For an ellipse, ρ_A is not a constant but can be calculated for a specified geometry as a function of the contact position [12][13]. As a result, v_{roll} depends on the flexion angle θ . As observed in [11], the sliding velocity v_{slide} also depends on θ :

$$v_{slide}(\theta) = ds_{slide} / dt = (ds_{slide} / d\theta) \omega \quad (2)$$

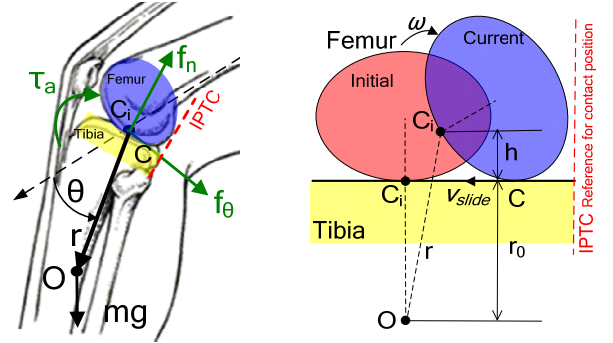
where the sliding displacement s_{slide} can be obtained from the difference between MRI data and the bio joint kinematics without sliding.

Knee joint kinematics

Using a lumped-parameter approach for describing the knee motion, the lower limb (leg and foot) is characterized by the mass centered at O in the polar coordinate system (r, θ) with its origin assigned at the *initial* contact point C_i on the femur as shown in Fig. 2, where the reference axis ($\theta = 0$) is along the longitudinal axis of the femur. As shown in Fig. 2(b) which illustrates the knee joint model, the distance OC_i is a constant r_0 . Because the translational motion is relatively small compared to the length of tibia,

$$r \approx r_0 + h \text{ and thus } \dot{h} = \dot{r}$$

which corresponds to the dynamic effects of the joint clearance. As shown in Fig. 2(b), the distance h between O and C is perpendicular to the contact plane, and a function of flexion angles. For the purpose of deriving $h(\theta)$ using data observed in [11], the contact point is referenced from the ipsilateral posterior tibial cortices (IPTC).



(a) Internal joint force/torque (b) Illustrative approximation
Fig. 2. Coordinate and free body diagram

For a relatively smooth rotation $\dot{\omega} \approx 0$, the knee joint kinematics can be computed from (3a, b) once $h(\theta)$ is known:

$$\dot{r} = (dh / d\theta) \omega; \text{ and } \ddot{r} = (d^2h / d\theta^2) \omega^2 \quad (3a, b)$$

The corresponding motion trajectory of the mass center O in the polar coordinate can be computed in terms of the flexion angle θ from equations (4a, b, and c):

$$\mathbf{r} = r \mathbf{e}_r; \quad \mathbf{v} = \dot{r} \mathbf{e}_r + r\dot{\theta} \mathbf{e}_\theta \quad (4a, b)$$

$$\mathbf{a} = (\ddot{r} - r\dot{\theta}^2) \mathbf{e}_r + (2\dot{r}\dot{\theta} + r\ddot{\theta}) \mathbf{e}_\theta \quad (4c)$$

Knee joint kinetics

From the Newton's 2nd law, the equations of motion describing the calf dynamics with respect to the upper limb are given by (5a, b):

$$m\mathbf{a} = \mathbf{f}_g + \mathbf{f}_\theta + \mathbf{f}_n + \mathbf{f}_r \quad (5a)$$

$$(J\ddot{\theta} + 2mr\dot{\theta})\mathbf{k} = \boldsymbol{\tau}_g + \boldsymbol{\tau}_a + \boldsymbol{\tau}_r \text{ where } \mathbf{k} = \mathbf{e}_r \times \mathbf{e}_\theta \quad (5b)$$

In (5a), m is the calf mass; \mathbf{f}_g is the gravity force; and \mathbf{f}_n and \mathbf{f}_θ are the forces exerted by the surrounding (muscle and ligament) tissues in \mathbf{e}_r and \mathbf{e}_θ directions respectively. For rehabilitation applications we include the term \mathbf{f}_r in (5a) to

account for the force exerted by an external device (such as an exoskeleton or a compliant sensor element). In (5b), J is the moment of inertia; τ_g and τ_r denote the torques due to the gravity and external device respectively; and τ_a is a net torque accounting for \mathbf{f}_n , \mathbf{f}_θ , and tissue contraction within the knee.

In (5b), the 1st term on the left hand side accounts for the leg rotation, while the 2nd term describes the interaction between $\dot{\theta}$ and \dot{r} due to the joint clearance. For a relatively smooth rotation $\ddot{\theta} = 0$, the $J\ddot{\theta}$ term can be neglected, which reduces the vector equations (5a, b) to three scalar equations (6a, b, c):

$$m(\ddot{r} - r\dot{\theta}^2) = f_g \sin \theta + f_n + f_{rr}(\theta) \quad (6a)$$

$$2mr\dot{\theta} = f_g \cos \theta + f_\theta + f_{r\theta}(\theta) \quad (6b)$$

$$2mr\dot{\theta} = \tau_g + \tau_a + \tau_r(\theta) \quad (6c)$$

Equation (6) provides a means to solve the inverse dynamics for the three unknowns (f_θ , f_n , τ_a).

B. Illustrative kinematic analysis of a human knee joint

The inverse dynamics (6) require its bio-joint kinematics. To understand the effect of the geometrical approximations on the contact point (between the femoral condyle and tibia) and account for the sliding velocity, three models are simulated and compared against published data [11]:

Model 1: Two sequential circles roll a flat plane [11].

Model 2: Ellipse rolls on a flat plane without sliding.

Model 3: Ellipse rolls on a flat plane with sliding.

The dimensions of the approximated circles [11] and ellipse (Fig. 1a) are listed in Table 1, where the contact point is referenced from the IPTC. The simulated results are given as a function of flexion angle in Figs. 3 and 4.

Table 1 Geometry approximation

Circles [11]		Ellipses	
$r_1 = 21\text{mm}$	$r_2 = 32\text{mm}$	$r_{maj} = 25.3\text{mm}$	$r_{min} = 21.1\text{mm}$
Initial contact position = 27mm; Angular velocity $\omega = 1.57\text{ rad/s}$			

In Fig. 3, the contact point positions are the horizontal distance of C from the IPTC in Fig. 1(a). Figure 4 shows the rolling velocity (1) and the sliding velocity (2) as well as their ratio v_{roll}/v_{slide} based on Model 3. Some observations in Figs 3 and 4 are discussed as follows:

a) In Model 1, the velocity ratio v_{roll}/v_{slide} is given as 1.7 [11]. For each rolling circle, the sliding velocity is assumed constant and thus, the contact point position is a linear function of θ . As shown in Fig. 3, the overall result, however, is not a smooth curve due to the transition from circles r_2 to r_1 .

Some discrepancies between the 2-circle model and experimental results can be observed when $\theta > 90^\circ$. This is because the rotational axis of the circle is tilted by a small angle. When projected on the camera plane, the tilted circle is essentially shown as an ellipse.

b) Based on the above observation, we model bio-joints [12] using ellipsoidal surfaces as they offer a more realistic

characterization than a multi-circle model, and are mathematically differentiable. As shown in Fig. 3 which compares Models 2 and 3 against experimental data, both sliding and rolling must be considered in the knee joint kinematics. Model 3 is used for the subsequent analysis.

c) The sliding displacement $s_{slide}(\theta)$ is obtained by subtracting the results of Model 2 from the experimental data in Fig. 3.

$$s_{slide}(\theta) / r_{maj} = 0.113\theta^4 - 0.358\theta^3 + 0.098\theta^2 + 0.876\theta \quad (7)$$

The corresponding v_{slide} can then be obtained from (2). As shown in Fig. 4, the v_{roll}/v_{slide} ratio is not a constant but its average value of 1.68 closely agrees with the experimental observation [11] of 1.7. Similarly,

$$h(\theta) / r_{maj} = -0.107\theta^3 + 0.493\theta^2 + 0.146\theta \quad (8)$$

With $h(\theta)$, \dot{r} and \ddot{r} in the inverse dynamic model (6) can be computed from (3a) and (3b) respectively.

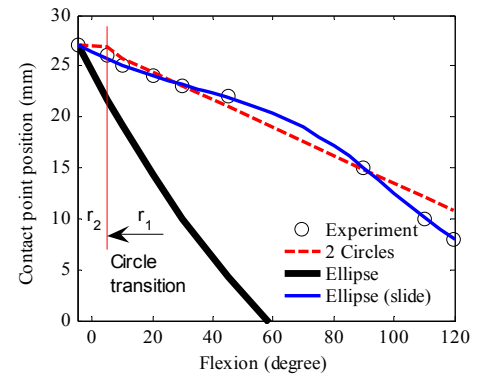
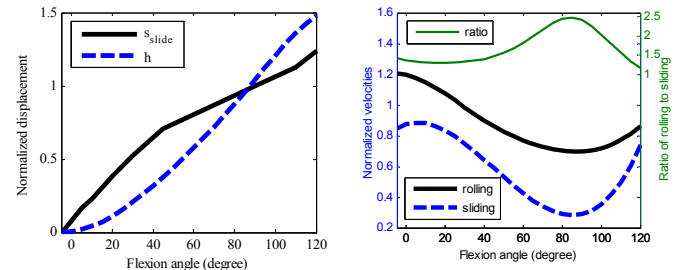


Fig. 3. Comparison of contact positions



(a) Characteristic joint displacements (b) Rolling and sliding velocities
Fig. 4. Results illustrating knee joint kinematics (Model 3)

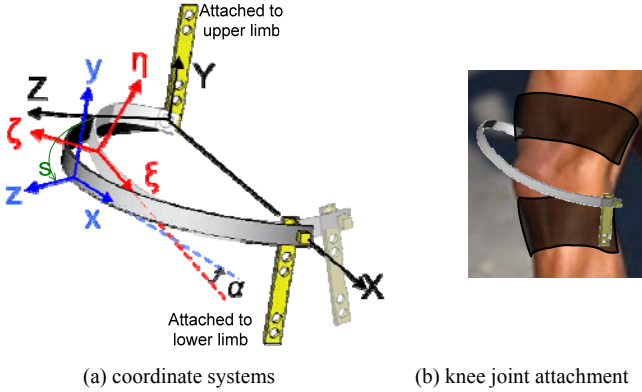
III. 3D COMPLIANT RING MECHANISMS

Compliance mechanisms that account for the bio-joint kinematics can be used as a knee sensor to measure the flexion angle θ and hence the internal forces/torque (f_θ , f_n , τ_a) from the inverse dynamics (6).

A. Design concept of compliant ring sensor

Figure 5 illustrates a compliant half-ring mechanism (between the lower and upper limbs) for a human knee joint. The half-circle twisting-ring [14] has been chosen for illustration because it has a number of applications in mechatronics. As shown in Fig. 5(b), one end is rigidly attached to the thigh. The other end is connected through a prismatic joint to the calf such that the flexion angle θ can be determined from the location of the free end (calf) relative to the fixed end (thigh) of the compliant ring.

The coordinate systems for design analysis of the compliant beam are defined in Fig. 1(a), where XYZ is a fixed reference frame; xyz and $\xi\eta\zeta$ are the orthogonal curvilinear frames for describing the initial and deformed shape respectively. The x and ζ axes are along the un-deformed and deformed reference axes of the beam respectively. The y and z axes are in the principal directions of the observed cross section area. Similarly, η and ζ correspond to y and z but in the deformed configuration. Without loss of generality, we assume that the reference axis passes through the center of the (rectangular) cross section in the following illustration.



(a) coordinate systems (b) knee joint attachment
Fig. 5. Human knee joint with a 3D compliant ring

As shown in Fig. 2(b), C_i is the initial contact point, and h is the normal distance of C_i on the femur to the (tibia) plane, the distance moved along the tibia $s_C = C_iC$ where C is the current contact point. For the rotation angle θ , the end point (X_e, Y_e, Z_e) of the compliant ring is constrained such that X_e freely slides along the x -axis while Y_e and Z_e are given by

$$Y_e = h \cos \theta - s_{slide} \cos \theta \tan \theta, \quad Z_e = h \sin \theta \quad (9)$$

The interest here is to find the flexion angle θ and the internal forces/torque vector (f_θ, f_n, τ_a) by measuring X_e along with the models of the complaint ring, and the inverse dynamics (6). Thus, in formulating a quasi-static model for the compliant ring, the flexion angle θ and the displacements (Y_e, Z_e) are specified as boundary conditions for solving X_e and the force $\mathbf{F} = [F_1, F_2, F_3]^T$ and moment $\mathbf{M} = [M_1, M_2, M_3]^T$ at the end point ($s = \pi R$). The internal forces/torque vector (f_θ, f_n, τ_a) can be calculated from (6), where the forces/torque $(f_{rr}, f_{r\theta}, \tau_r)$ acting by the sensor are given by (10)

$$\begin{bmatrix} f_{rr} \\ f_{r\theta} \\ \tau_r \end{bmatrix} = \begin{bmatrix} -\cos \theta & -\sin \theta & 0 \\ \sin \theta & -\cos \theta & 0 \\ -v & R + w & 1 \end{bmatrix} \begin{bmatrix} F_1 \\ F_2 \\ M_3 \end{bmatrix} \quad (10)$$

B. Quasi-static model of a compliant beam

The initial curved shape is described by (11):

$$\frac{d}{ds} [\mathbf{i}_x \quad \mathbf{i}_y \quad \mathbf{i}_z]^T = \mathbf{k} \times [\mathbf{i}_x \quad \mathbf{i}_y \quad \mathbf{i}_z]^T \quad (11)$$

where the unit vectors $\mathbf{i}_x, \mathbf{i}_y$ and \mathbf{i}_z are along the axes x, y and z ; and $\mathbf{i}_1, \mathbf{i}_2$ and \mathbf{i}_3 along the axes ζ, η and ξ ; s is the undeformed arc length from the root of the beam to the reference point on the observed cross section; and $\mathbf{k} = [k_1, k_2, k_3]^T$ describes the initial curvatures.

Kinematics

The deformed and un-deformed coordinate systems are related by a rotational matrix $[\mathbf{T}]$:

$$[\mathbf{i}_1 \quad \mathbf{i}_2 \quad \mathbf{i}_3]^T = [\mathbf{T}][\mathbf{i}_x \quad \mathbf{i}_y \quad \mathbf{i}_z]^T \quad (12)$$

where $[\mathbf{T}]^T = [\mathbf{T}_1 \quad \mathbf{T}_2 \quad \mathbf{T}_3]$; and $\mathbf{T}_i = [T_{i1} \quad T_{i2} \quad T_{i3}]^T$. Because of the orthogonal property $[\mathbf{T}]^T = [\mathbf{T}]^{-1}$, $[\mathbf{T}]$ can be written as

$$[\mathbf{T}] = \begin{bmatrix} 1 & 0 & 0 \\ 0 & \cos \varphi & \sin \varphi \\ 0 & -\sin \varphi & \cos \varphi \end{bmatrix} [\mathbf{B}(\alpha)] \quad (13)$$

where φ is an Euler angle for twisting about the ζ axis; and the transformation matrix $[\mathbf{B}(\alpha)]$ is due to the bending rotation α as shown in Fig. 6. In (12),

$$\cos \alpha = T_{11} = \mathbf{i}_1 \cdot \mathbf{i}_x; \quad \sin \alpha = |\mathbf{i}_1 \times \mathbf{i}_x| = \sqrt{T_{12}^2 + T_{13}^2}. \quad (14a, b)$$

For $0^\circ \leq \alpha < 180^\circ$ ($T_{11} \neq -1$), $[\mathbf{B}(\alpha)]$ is given in terms of \mathbf{T}_1 and φ in (12) [14][15]:

$$[\mathbf{B}(\alpha)] = \begin{bmatrix} T_{11} & T_{12} & T_{13} \\ -T_{12} & T_{11} + T_{13}^2 / (1 + T_{11}) & -T_{12}T_{13} / (1 + T_{11}) \\ -T_{13} & -T_{12}T_{13} / (1 + T_{11}) & T_{11} + T_{12}^2 / (1 + T_{11}) \end{bmatrix} \quad (15)$$

$$\text{Since } \|\mathbf{T}_1\| = T_{11}^2 + T_{12}^2 + T_{13}^2 = 1 \quad (16)$$

only three of the four variables (T_{11}, T_{12}, T_{13} and φ) in $[\mathbf{T}]$ are independent.

Governing equations

For negligible torsional warping, the axial strain e and the curvatures after deformation $\boldsymbol{\rho} = [\rho_1, \rho_2, \rho_3]^T$ can be expressed using the following relationship [15]:

$$\begin{bmatrix} e \\ \boldsymbol{\rho} \end{bmatrix} = \text{diag} \left[\frac{1}{EA}, \frac{1}{GJ}, \frac{1}{EI_{22}}, \frac{1}{EI_{33}} \right] \begin{bmatrix} F_1 \\ \mathbf{M} \end{bmatrix} + \begin{bmatrix} 0 \\ \mathbf{k} \end{bmatrix} \quad (17)$$

where E is the elastic modulus; G is the shear modulus; A is the cross section area; J is the polar moment of inertia; and I_{22} and I_{33} are the moments of inertia.

The force and moment equations for the 3D compliant beam are given by (18a) and (18b) respectively:

$$\mathbf{F}' = -\boldsymbol{\rho} \times \mathbf{F} - [\mathbf{T}] \mathbf{q}_F \quad (18a)$$

$$\mathbf{M}' = -\boldsymbol{\rho} \times \mathbf{M} - (1 + e) [0 \quad -F_3 \quad F_2]^T - \mathbf{q}_M \quad (18b)$$

where $\mathbf{F} = [F_1, F_2, F_3]^T$ and $\mathbf{M} = [M_1, M_2, M_3]^T$ are the force and moment in terms of $\xi\eta\zeta$ coordinates respectively; the derivatives (denoted by ') is taken with respect to the path length s ; \mathbf{q}_F are distributed forces acting along the axes x, y and z ; and \mathbf{q}_M are the distributed moments acting along the axes ζ, η and ξ . From (11) to (15), we have

$$\mathbf{T}' = \boldsymbol{\rho}_3 \mathbf{T}_2 - \boldsymbol{\rho}_2 \mathbf{T}_3 - \mathbf{k} \times \mathbf{T}_1 \quad (18c)$$

$$[1 + u' \quad v' \quad w']^T = \mathbf{k} \times [u \quad v \quad w]^T + (1 + e) \mathbf{T}_1 \quad (18d)$$

$$\varphi' = \rho_1 - \mathbf{k} \cdot \mathbf{T}_1 - (T_{13}T'_{12} - T_{12}T'_{13}) / (1 + T_{11}) \quad (18e)$$

where u, v and w are the displacements of the observed reference point in the directions of axes x, y and z respectively.

For the application in Fig. 5, the boundary conditions (BCs) are given in Fig. 6. The four vector and one scalar equations, (18a-e), are governing equations for solving the 13 unknowns ($F_1, F_2, F_3; M_1, M_2, M_3; T_{11}, T_{12}, T_{13}; u, v, w; \varphi$); 12 of them are independent. The boundary condition problem (BVP) characterized by (18) can be recast as an initial value problem (IVP) and solved using a multiple shooting method (MSM) [16] as summarized in the Appendix. To solve using the MSM, the (guessed) values of the six force/moment component variables (F_i and $M_i, i=1, 2$ and 3) at $s=0$ must also be specified as initial conditions.

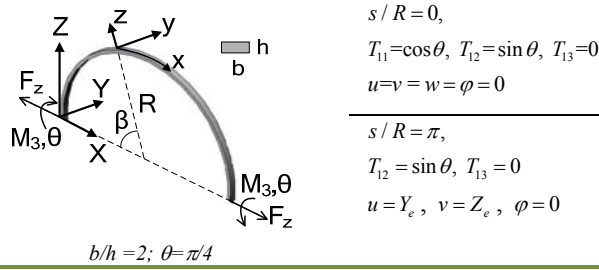


Fig. 6. Boundary conditions of the half-circle twist ring

IV. ILLUSTRATIVE EXAMPLES AND RESULTS

To provide intuitive insights the effects of material properties, aspect ratios (b/h), and the end-point (Y_e, Z_e) displacements on the ring deformation, the following illustrative examples are analyzed numerically:

1. Compliant ring only ($Y_e=Z_e=0$): The flexion angle θ is specified resulting in twisting the ring at ($\beta=0, \pi$).
 - (a) Effect of cross-sectional aspect ratio
 - (b) Effect of different materials
2. Combined compliant ring and knee joint, where the end-point (Y_e, Z_e) displacements are specified with (9) in addition to the flexion angle θ .

Example 1: Effect of aspect ratios and materials ($Y_e=Z_e=0$)

For design purposes, the results are presented in non-dimensional forms; the bases of the normalization are tabulated in Table 2. The deformed shape of the compliant ring ($b/h=2$) subject to a pure twisting of $\theta=\pi/4$ at both ends is shown in Fig. 7. The effects of aspect ratios ($b/h=2, 3, 6$), and four different materials (steel, titanium, aluminum and delrin) on the (normalized) twisting moment M_3 at the ends are compared in Fig. 8. Numerical values of the characteristic parameters for the four materials are compared in Table 3.

Table 2 Basis of normalization

Geometry	Displacement	Force	Moment
$R, b/h$	$u, v, w \sim R$	$F \sim EI_{33} / R^2$	$M \sim EI_{33} / R$
	$k, \rho \sim 1/R$	$q_f \sim EI_{33} / R^3$	$q_m \sim EI_{33} / R^2$

Table 3 Material properties

Parameters	Steel	Titanium	Aluminum	Delrin
E (GPa)	193	116	70	3.1
Poisson ratio	0.25	0.34	0.3	0.35
Density (10^3kg/m^3)	7.85	4.54	2.7	1.42

As shown in Fig. 8, the effect of different materials is relatively insensitive on the *normalized* twisting moment M_3 at the ends. However, different normalized M_3 curves are needed for different aspect ratios (b/h).

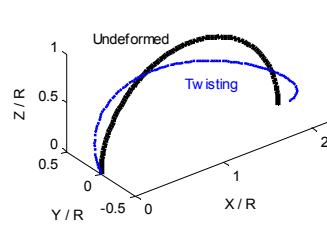


Fig. 7. Normalized deformed shape of the twisted compliant ring

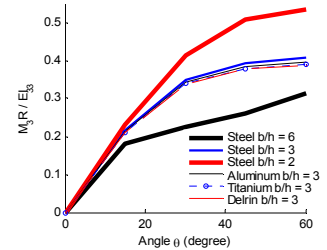


Fig. 8. Effect of aspect ratios and materials

Example 2: Effect of flexion end on combined compliant ring and knee joint ($Y_e \neq 0, Z_e \neq 0$)

The compliant ring is connected to the knee joint as shown in Fig. 5. Numerical values characterizing a human lower extremity and the compliant ring geometry used in this example are given in Table 4 [17]. The combined mass of the rotational part (lower leg/foot) is 3.62kg and its normal distance r_0 from the center O to the contact plane is 0.2453m .

The following computational procedure is used:

- Step 1: For a given θ , calculate Y_e and Z_e from (9).
- Step 2: Solve (18) with boundary conditions given in Fig. 6.
- Step 3: Obtain $X_e = w, \mathbf{F} = [F_1, F_2, F_3]^T$ and $\mathbf{M} = [M_1, M_2, M_3]^T$ for the end $s = \pi R$.
- Step 4: Calculate $f_{rr}, f_{r\theta}$ and τ_r from (10).
- Step 5: Calculate f_n, f_θ and τ_a from (6).
- Step 6: Repeat Steps 1 to 5 for different θ .

Table 4 Physical parameters of human's lower limb

Human	Length (m)	Mass (kg)
Upper leg	0.40	7.02
Lower leg/foot	0.37/0.27	2.44/1.18
Stainless steel ring		
$R=76.2 \text{mm}$	$b=6.35 \text{mm}$	$h=0.635 \text{mm}$

Figure 9, which graphs the end-point displacements (X_e, Y_e, Z_e) of the half-circle ring as a function of the flexion angle θ , shows that the knee flexion angle θ can be determined from the translation X_e by a displacement sensor system. To determine the extra effort needed to overcome the added stiffness due to the compliant ring, we compare the internal forces/torque vector (f_θ, f_n, τ_a) with and without wearing the compliant ring mechanism in Fig. 10. For a flexion angle of less than 90° , the maximum percentage errors for f_n, f_θ and τ_a are 3.7%, 14.5% and 1.2% respectively. As compared in Fig. 10, the compliant ring mechanism has little effect on the internal forces and torque in the knee joint.

V. CONCLUSIONS

A general method of modeling the kinematics and kinetics of a human knee joint has been presented, which provides a means to account for the transition within the clearance of the

joint. This method does not assume a fixed rotational axis and thus more realistically characterizes a bio-joint. The ellipsoidal bio-joint model derived from published MRI data, which is mathematically differentiable, has been applied to design of a three dimensional (3D) compliant half-circle mechanism. The effects of materials and the aspect ratios (of the mechanism with a rectangular cross section) on the design are presented. The design of a compliant sensing mechanism is numerically analyzed with boundary conditions derived from the knee joint model. The results have demonstrated the concept feasibility of obtaining the rotation angle of a human knee joint by measuring translational motion displacement of the compliant sensing mechanism.

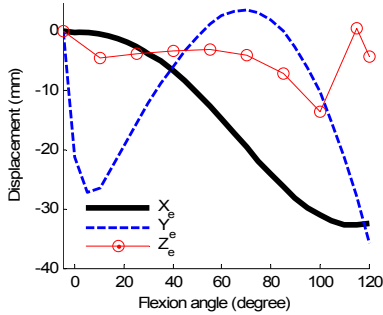


Fig. 9. End-point displacements (X_e, Y_e, Z_e)

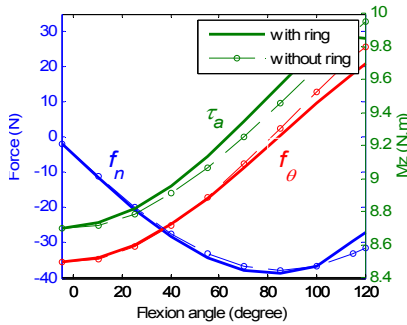


Fig. 10. Effect of compliant ring on the internal force/torque vector

APPENDIX Multiple shooting method (MSM)

The boundary condition problem (BVP) of a 3D compliant beam can be written in the following form:

$$\mathbf{X}' = \mathbf{f}(s, \mathbf{X}), \quad \mathbf{g}(\mathbf{X}(0), \mathbf{X}(L)) = \mathbf{0} \quad (\text{A.1})$$

where \mathbf{X} is a vector of the 13 variables; $0 \leq s \leq L$ with L being the beam length; and $\mathbf{g}(\bullet)$ is the boundary conditions (BCs) specifying the geometrical loading constraints at both ends. The BVP (A.1) is recast as an initial value problem (IVP) and solved using a MSM [16]. For this, the region $[0, L]$ is divided into $m-1$ sections by m nodes as shown in Fig. A, where s_i is the arc length from the root of the beam to the i^{th} node; $\mathbf{x}_i^{(n)}$ is the initial guess for the i^{th} section, and the superscript (n) denotes the n^{th} guess.

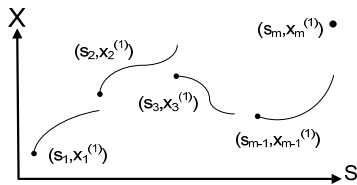


Fig. A. Multiple shooting method

The BVP can then be posed as a set of m 1st-order non-linear equations (A.2) subject to a set of m constraints (A.3) as functions of the initial guesses:

$$\mathbf{X}' = \mathbf{f}(s, \mathbf{X}), \quad \mathbf{X}(s_i) = \mathbf{x}_i^{(n)} \quad (\text{A.2})$$

$$\mathbf{C}(\mathbf{x}^{(n)}) := \begin{bmatrix} \mathbf{C}_1(\mathbf{x}_1^{(n)}, \mathbf{x}_2^{(n)}) \\ \vdots \\ \mathbf{C}_{m-1}(\mathbf{x}_{m-1}^{(n)}, \mathbf{x}_m^{(n)}) \\ \mathbf{C}_m(\mathbf{x}_1^{(n)}, \mathbf{x}_m^{(n)}) \end{bmatrix} := \begin{bmatrix} \mathbf{X}(s_2; s_1, \mathbf{x}_1^{(n)}) - \mathbf{x}_2^{(n)} \\ \vdots \\ \mathbf{X}(s_m; s_{m-1}, \mathbf{x}_{m-1}^{(n)}) - \mathbf{x}_m^{(n)} \\ \mathbf{g}(\mathbf{x}_1^{(n)}, \mathbf{x}_m^{(n)}) \end{bmatrix} \quad (\text{A.3})$$

Using Newton method, the initial guesses are updated using (A.4):

$$\mathbf{x}^{(n+1)} = \mathbf{x}^{(n)} - \alpha [\mathbf{DC}(\mathbf{x}^{(n)})]^{-1} \mathbf{C}(\mathbf{x}^{(n)}), \quad n = 0, 1, \dots \quad (\text{A.4})$$

where $\mathbf{DC} = \partial \mathbf{C} / \partial \mathbf{x}^{(n)}$ is a matrix, α is a coefficient for the iteration step size. The iteration process of (A.4) stops until $\mathbf{C}(\mathbf{x}^{(n)}) \rightarrow \mathbf{0}$ (or a small tolerance error Err_{tol}) implying that the solution is continuous and satisfies the BCs. The MSM can be implemented using the following steps:

1. Set the initial guess $\mathbf{x}^{(0)} = [\mathbf{x}_1^{(0)} \quad \mathbf{x}_2^{(0)} \quad \dots \quad \mathbf{x}_m^{(0)}]$.
2. Solve the IVP (9a) with $\mathbf{X}(0) = \mathbf{x}^{(0)}$.
3. Calculate the residual $\|\mathbf{C}(\mathbf{x}^{(0)})\|$ and corresponding $\mathbf{DC} = \partial \mathbf{C} / \partial \mathbf{x}^{(0)}$.
4. Update the initial guess by (A.4).
5. Repeat steps 2-4 (replacing $\mathbf{x}^{(0)}$ with $\mathbf{x}^{(n)}$) until $\|\mathbf{C}(\mathbf{x}^{(n)})\| < \text{tolerance error } Err_{tol}$.

REFERENCES

- [1] K. E. Gordon, D. P. Ferris "Learning to walk with a robotic ankle exoskeleton," *J. of Biomechanics*, vol. 40, no. 12, pp. 2636-2644, 2007.
- [2] G. Colombo, M. Joerg, R. Schreier, V. Dietz, "Treadmill training of paraplegic patients using a robotic orthosis," *J. of Rehabilitation Research and Development*, vol. 37, no. 6, pp. 693-700, 2000.
- [3] A. B. Zoss, H. Kazerooni, A. Chu, "Biomechanical design of the Berkeley lower extremity exoskeleton (BLEEX)," *IEEE/ASME Trans. on Mechatronics*, vol. 11, no. 2, pp. 128-138, 2006.
- [4] H. Kawamoto, Y. Sankai, "Power assist method based on Phase Sequence and muscle force condition for HAL," *Advanced Robotics*, vol. 19, no. 7, pp. 717-734, 2005.
- [5] D. P. Ferris, J. M. Czerniecki, B. Hannaford, "An ankle-foot orthosis powered by artificial pneumatic muscles," *J. of Applied Biomechanics*, vol. 21, no. 2, pp. 189-197, 2005.
- [6] K. Kiguchi, K. Iwami, M. Yasuda, K. Watanabe, T. Fukuda, "An exoskeletal robot for human shoulder joint motion assist," *IEEE/ASME Trans. on Mechatronics*, vol. 8, no. 1, pp. 125-135, 2003.
- [7] M. Bouzit, G. Burdea, G. Popescu, R. Boian, "The Rutgers Master II - New design force-feedback glove," *IEEE/ASME Trans. on Mechatronics*, vol. 7, no. 2, pp. 256-263, 2002.
- [8] N. G. Tsagarakis, D. G. Caldwell, "Development and control of a 'soft-actuated' exoskeleton for use in physiotherapy and training," *Autonomous Robots*, vol. 15, no. 1, pp. 21-33, 2003.
- [9] J. F. Veneman, R. Ekkelenkamp, R. Kruidhof, F. C. T. van der Helm, H. van der Kooij, "A series elastic- and Bowden-cable-based actuation system for use as torque actuator in exoskeleton-type robots," *Int. J. of Robotics Research*, vol. 25, no. 3, pp. 261-281, 2006.
- [10] K. H. Low, "Initial experiments on a leg mechanism with a flexible geared joint and footpad," *Advanced Robotics*, vol. 19, no. 4, pp. 373-399, 2005.
- [11] H. Iwaki, V. Pinskerova, M. A. R. Freeman, "Tibiofemoral movement 1: the shapes and relative movements of the femur and tibia in the unloaded cadaver knee," *J. of Bone & Joint Surgery*, vol. 82-B, no. 8, 2000.
- [12] K.-M. Lee, J. Guo, "Biological joint kinematic model for flexible deboning automation," *Int. Symp. on Flexible Automation*, Atlanta GA, USA June 23-26, 2008.
- [13] J. Guo, K.-M. Lee, "Effects of musculoskeleton model on flexible deboning automation," *Int. Symp. on Flexible Automation*, Atlanta GA, USA June 23-26, 2008.
- [14] K. Alkire, "An analysis of rotor blade twist variables associated with different Euler sequences and pretwist treatments," *NASA TM 84394*, 1984.
- [15] P. F. Pai, A. N. Palazotto, "Large-deformation analysis of flexible beams," *Int. J. of Solids Structures*, vol. 33, no. 9, pp. 1335-1353, 1996.
- [16] J. Stoer, R. Bulirsch, *Introduction to Numerical Analysis*, pp. 476-477, Springer-Verlag, New York, 1980.
- [17] T. Nomiya, A. Lawi, T. Katsuhara, S. Hirokawa, "Model analysis of lower limb at deep knee flexion," *Int. Conf. on Elect. Eng. and Informatics*, Institut Teknologi Bandung, Indonesia, June 17-19, 2007.